A Collocation–Galerkin Finite Element Model of Cardiac Action Potential Propagation

Jack M. Rogers and Andrew D. McCulloch

Abstract— **A new computational method was developed for modeling the effects of the geometric complexity, nonuniform muscle fiber orientation, and material inhomogeneity of the ventricular wall on cardiac impulse propagation. The method was used to solve a modification to the FitzHugh–Nagumo sytem of equations. The geometry, local muscle fiber orientation, and material parameters of the domain were defined using linear Lagrange or cubic Hermite finite element interpolation. Spatial variations of time-dependent excitation and recovery variables were approximated using cubic Hermite finite element interpolation, and the governing finite element equations were assembled using the collocation method. To overcome the deficiencies of conventional collocation methods on irregular domains, Galerkin equations for the no-flux boundary conditions were used instead of collocation equations for the boundary degrees-of-freedom. The resulting system was evolved using an adaptive Runge–Kutta method. Converged two-dimensional simulations of normal propagation showed that this method requires less CPU time than a traditional finite difference discretization. The model also reproduced several other physiologic phenomena known to be important in arrhythmogenesis including: Wenckebach periodicity, slowed propagation and unidirectional block due to wavefront curvature, reentry around a fixed obstacle, and spiral wave reentry. In a new result, we observed wavespeed variations and block due to nonuniform muscle fiber orientation. The findings suggest that the finite element method is suitable for studying normal and pathological cardiac activation and has significant advantages over existing techniques.**

I. Introduction

A DETAILED understanding of the global activation and recovery patterns underlying cardiac arrhythmias has been elusive—largely because of the geometric and structural complexity of the heart and the fine spatial scale of the activation patterns relative to the size of the whole organ. Recent progress has come through large-scale computerized electrode mapping experiments that have clearly demonstrated the role of reentry in ventricular tachycardia (VT) and fibrillation (VF) [1]–[4]. However, the resolution of these experiments is fundamentally limited by the number of available recording electrodes and the tissue damage they cause.

Computer models can help in the interpretation of sparse mapping data, suggest new experiments, and provide insights into the physics of cardiac action potential propagation. Numerous models have been developed [5], [6]. Many use the cellular automata approach in which propagation is governed by a set of arbitrary rules [7]–[11]. Several have shown that reentry can be initiated by a premature wave propagating across a region with spatially nonuniform refractoriness. These models are appealing because of their simplicity and computational speed; however, the rule-based approach is not an accurate model of the biophysics of cardiac activation. Another approach uses numerical and analytic models of generic excitable media to study the large-scale geometry of excitation waves. By adopting simple but qualitatively realistic representations of spatial communication and membrane kinetics, such models have aided our understanding of the initiation and subsequent dynamics of reentrant spiral waves in excitable media [12]–[14].

Recently, there has been a trend toward models that more closely reflect the biophysics of cardiac action potential propagation. They address three main properties: the biochemical events in the cell membrane that generate the action potential, the microstructural basis of cell–cell coupling, and the large-scale geometric complexity, fibrous architecture, and spatial inhomogeneity of the whole organ. Sophisticated models of the membrane dynamics of the cardiac cell have been developed [15], [16], as have models which explore the effects of the tissue microstructure on action potential propagation [17]–[21]. However, the effects of the large-scale geometric complexity of the heart have remained largely unexplored, probably because of the lack of feasible computational methods to cope with such simulations.

The objective of this work was to develop a model to study the effects of the heart's geometric complexity, nonuniform anisotropy, and material inhomogeneity. Because finite difference methods are not well suited to this problem, we describe a new collocation–Galerkin finite element method capable of solving continuous reaction–diffusion equations on such complex domains. This model is designed to form the basis for increasingly sophisticated quantitative simulations of the electrical activity of the heart. Our first objective is to explore the effects of these geometric factors on generic action potential propagation and to generate experimentally testable predictions of the behavior of myocardium. We show that our model produces converged traveling-wave solutions to a modification of the well-known FitzHugh–Nagumo system of equations for excitable media [22]. Two-dimensional simulations demonstrate that the model can efficiently reproduce normal propagation as well as several phenomena thought to be important in arrhythmogenesis.

Manuscript received August 31, 1992; revised February 25, 1994. This work was supported by NIH Grants HL41603 and HL43023, Doctoral Training Grant HL07089, and NSF PYI Grant BCS-91-57961.

J. M. Rogers is with the Institute for Biomedical Engineering, University of California at San Diego, La Jolla, CA 92093 USA and the San Diego Supercomputer Center, San Diego, CA 92186 USA.

A. D. McCulloch is with the Institute for Biomedical Engineering, University of California at San Diego, La Jolla, CA 92093 USA.

IEEE Log Number 9402542.

II. The Governing Equations

The model is based on the FitzHugh–Nagumo equations for excitable media [22]

$$\frac{\partial u}{\partial t} = \nabla \cdot \boldsymbol{D} \nabla u + c_1 u(u-a)(1-u) - c_2 v$$
$$\frac{\partial v}{\partial t} = b(u - dv)$$
with boundary condition
$$\frac{\partial u}{\partial \boldsymbol{n}} = 0. \tag{1}$$

In this reaction–diffusion system, u is the excitation variable, which can be identified with transmembrane potential, v is the recovery variable, $\boldsymbol{n}$ is a vector normal to the boundary, $\boldsymbol{D}$ is the diffusion tensor, and a, b, c_1, c_2, and d are "membrane" parameters that define the shape of the action potential pulse. The diffusion tensor and the parameters are constant in time, but not necessarily in space. These equations often appear in the literature in various equivalent forms [23].

The passive spread of current is governed by the diffusive term in the first equation, and the ionic currents are described by the second equation and the last two terms of the first equation. The cubic term governs activation. It has three fixed points at $u = 0, u = a$, and $u = 1$. The points $u = 0$ and $u = 1$ are stable and represent the resting and excited state, respectively. The excitation threshold is represented by the unstable point $u = a$. A point in the domain will tend toward $u = 0$ unless potential fluctuations exceed a. In this case, the point becomes excited and tends toward 1. The recovery variable v brings the system back to the rest state and prevents reexcitation for a certain refractory period. The appearance of u in the second equation makes recovery dependent on the potential of neighboring regions, and the linear dependence on v makes the time course of recovery first order. With a suitable choice of parameters, the local state oscillates among rest, excitation, and refractoriness. Thus, this parabolic system of partial differential equations can support a traveling-wave solution.

The solution waveform of the FHN system shows a negative excursion of u during the refractory part of the wave, where u is close to 0, but v is elevated (Fig. 1(a)). This hyperpolarization is not characteristic of the cardiac action potential, and may adversely affect the recovery properties of the model, particularly in the complex reentrant activation patterns that are of most interest. The hyperpolarization is eliminated (Fig. 1(b)) by modifying the last term in the first equation of (1)

$$\frac{\partial u}{\partial t} = \nabla \cdot \boldsymbol{D} \nabla u + c_1 u(u-a)(1-u) - c_2 uv$$
$$\frac{\partial v}{\partial t} = b(u - dv). \tag{2}$$

For both systems, the trajectory through the excitation/recovery cycle begins at a point in the phase plane where du/dt and dv/dt are both positive (Fig. 2). Excitation u increases rapidly until it crosses its nullcline. At this point, du/dt is negative, recovery begins, and u decreases until the trajectory again crosses a nullcline of u and begins the final path to the origin. In the unmodified FHN system (Fig. 2(a)), the trajectory encounters the second branch of the nullcline in the left half of the phase plane. The placement of this nullcline is responsible for the undershoot of u. However, in the modified FHN system (Fig. 2(b)), there is a nullcline of u at $u = 0$ that prevents the undershoot.

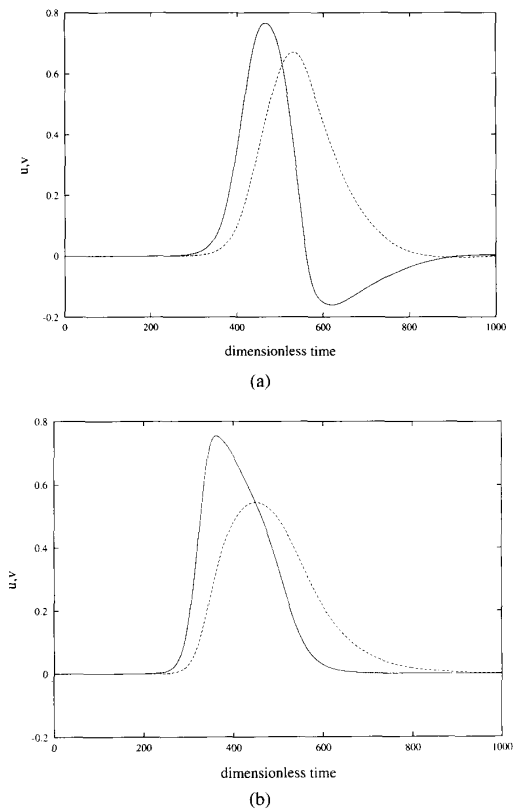

Fig. 1. Action potential waveforms for (a) the standard FHN system (1) and (b) the modified FHN system (2). Note the hyperpolarization of u in the recovery phase of (a). Solid line: the excitation variable u. Dashed line: the recovery variable v. Membrane parameters for the standard FHN system: $a = 0.12, b = 0.011, c_1 = 0.175, c_2 = 0.03, d = 0.55$. The membrane parameters for the modified FHN system are listed in Table I.

III. Solution Methods

A hybrid collocation–Galerkin finite element method was developed to solve the modified or unmodified FHN systems on a general domain with fibrous anisotropy. Although the implementation supports both two-dimensional (2-D) and three-dimensional (3-D) problems, for simplicity, only 2-D solutions are discussed in this paper.

A. Notation and Coordinate Systems

The following development makes use of general tensor notation [24]. Bold symbols denote vector or tensor quantities. Individual components of vectors and tensors are denoted with subscripted or superscripted indexes. Indexes repeated within a product imply summation over their range; however, indexes in parentheses are not summed. Thus, the term $a_i b^i$ expresses the inner product of the two vectors $\boldsymbol{a}$ and $\boldsymbol{b}$, while $a_{(i)} b^{(i)}$ is the product of individual components.

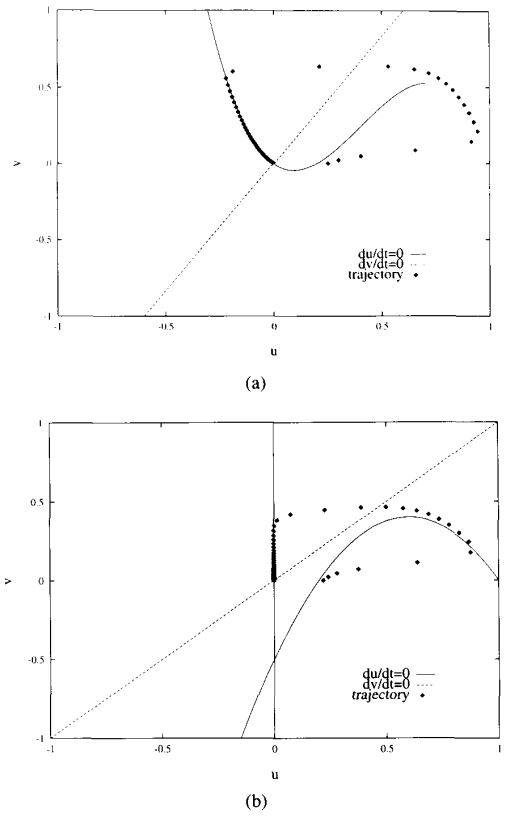

Fig. 2. Phase space trajectories of a single, spatially uncoupled point following (a) standard FHN kinetics (1) and (b) modified FHN kinetics (2). The nullclines of both u and v are plotted. The trajectories begin in the region of the phase plane where du/dt and dv/dt are both greater than 0 and proceed counterclockwise. Note that in (b), u has two nullclines.

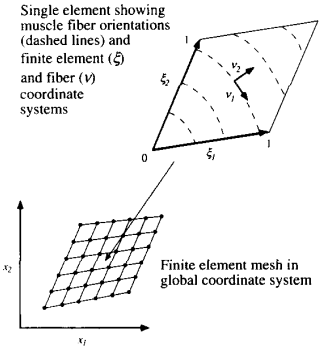

Fig. 3. The relationship among the global ($\boldsymbol{x}$), finite element ($\boldsymbol{\xi}$), and fiber ($\boldsymbol{\nu}$) coordinate systems.

We use three coordinate systems (Fig. 3). $\boldsymbol{x} = x^i \boldsymbol{i}_i$ is the world coordinate system, which in this paper is always Cartesian. The x^i are coordinates and the $\boldsymbol{i}_i$ are the base vectors of the coordinate system. $\boldsymbol{\xi} = \xi^l \boldsymbol{g}_l$ is the finite element coordinate system that is local to each element. The ξ^l coordinates range from 0 to 1 along each element edge, and the covariant base vectors $\boldsymbol{g}_l$ point in the direction of the coordinate axes and may be curvilinear and/or nonorthogonal. $\boldsymbol{\nu} = \nu^p \boldsymbol{a}_p$ is the orthonormal "fiber" coordinate system defined such that one axis is everywhere aligned with the cardiac muscle fibers (Appendix). Since the system is orthonormal, there is no difference between the covariant and contravariant base vectors ($\boldsymbol{a}_p = \boldsymbol{a}^p$). In this paper, the indexes i, j, and k are used to index the world coordinates; l, m, and n are used for finite element coordinates; and p, q, and r refer to the fiber coordinate system. These indexes all range from 1 to 2 in 2-D and from 1 to 3 in 3-D.

B. Finite Element Interpolation

The variables u and v, the local fiber orientation, the components of the diffusion tensor, the membrane parameters a, b, c_1, c_2, and d, and the global geometry of the finite element mesh (i.e., the global coordinates of points defined in the element ($\boldsymbol{\xi}$) coordinate systems) are all approximated by linear Lagrange or cubic Hermite finite element interpolation [25], [26]. In this scheme, the 2-D domain is subdivided into four-sided finite elements with nodes located at the vertices (Figs. 3, 4). The value of a variable within an element is interpolated from parameters defined at the nodes. These parameters are global in that they are shared by all adjacent elements. For linear Lagrange interpolation, the parameters are simply the values of the variable at the nodes. Thus, the bilinear approximation of some variable z within any element is obtained by mapping the appropriate global nodes to the nodes of the current element and using the interpolation function

$$z(\xi_1, \xi_2) = \begin{array}{l} L_1(\xi_1)\, L_1(\xi_2)\, z(0,0) \\ +L_2(\xi_1)\, L_1(\xi_2)\, z(1,0) \\ +L_1(\xi_1)\, L_2(\xi_2)\, z(0,1) \\ +L_2(\xi_1)\, L_2(\xi_2)\, z(1,1) \end{array} \tag{3}$$

where the 1-D linear Lagrange interpolating functions are $L_1(\xi) = 1 - \xi$ and $L_2(\xi) = \xi$.

Since the nodal parameters are the nodal values of the interpolated variable, linear Lagrange interpolation ensures interelement continuity of the variable (C^0 continuity). Continuity of the gradient of the variable as well as the variable itself (C^1 continuity) is achieved with cubic Hermite interpolation, which additionally uses the spatial derivatives of the variable as nodal parameters. In 2-D, there are four parameters per node, and the bicubic Hermite interpolation function for a variable z is

$$\begin{aligned} z(\xi_1, \xi_2) = {} & H_1^0(\xi_1)\, H_1^0(\xi_2)\, z(0,0) \\ & + H_2^0(\xi_1)\, H_1^0(\xi_2)\, z(1,0) \\ & + H_1^0(\xi_1)\, H_2^0(\xi_2)\, z(0,1) \\ & + H_2^0(\xi_1)\, H_2^0(\xi_2)\, z(1,1) \\ & + H_1^1(\xi_1)\, H_1^0(\xi_2) \left.\frac{\partial z}{\partial \xi_1}\right|_{(0,0)} \\ & + H_2^1(\xi_1)\, H_1^0(\xi_2) \left.\frac{\partial z}{\partial \xi_1}\right|_{(1,0)} \\ & + H_1^1(\xi_1)\, H_2^0(\xi_2) \left.\frac{\partial z}{\partial \xi_1}\right|_{(0,1)} \\ & + H_2^1(\xi_1)\, H_2^0(\xi_2) \left.\frac{\partial z}{\partial \xi_1}\right|_{(1,1)} \end{aligned}$$

$$
\begin{aligned}
&+ H_1^0(\xi_1)\, H_1^1(\xi_2) \left.\frac{\partial z}{\partial \xi_2}\right|_{(0,0)} \\
&+ H_2^0(\xi_1)\, H_1^1(\xi_2) \left.\frac{\partial z}{\partial \xi_2}\right|_{(1,0)} \\
&+ H_1^0(\xi_1)\, H_2^1(\xi_2) \left.\frac{\partial z}{\partial \xi_2}\right|_{(0,1)} \\
&+ H_2^0(\xi_1)\, H_2^1(\xi_2) \left.\frac{\partial z}{\partial \xi_2}\right|_{(1,1)} \\
&+ H_1^1(\xi_1)\, H_1^1(\xi_2) \left.\frac{\partial^2 z}{\partial \xi_1 \partial \xi_2}\right|_{(0,0)} \\
&+ H_2^1(\xi_1)\, H_1^1(\xi_2) \left.\frac{\partial^2 z}{\partial \xi_1 \partial \xi_2}\right|_{(1,0)} \\
&+ H_1^1(\xi_1)\, H_2^1(\xi_2) \left.\frac{\partial^2 z}{\partial \xi_1 \partial \xi_2}\right|_{(0,1)} \\
&+ H_2^1(\xi_1)\, H_2^1(\xi_2) \left.\frac{\partial^2 z}{\partial \xi_1 \partial \xi_2}\right|_{(1,1)} \qquad (4)
\end{aligned}
$$

where the 1-D Hermite basis functions are

$$
\begin{aligned}
H_1^0(\xi) &= 1 - 3\xi^2 + 2\xi^3 \qquad & H_1^1(\xi) &= \xi(\xi - 1)^2 \\
H_2^0(\xi) &= \xi^2(3 - 2\xi) \qquad & H_2^1(\xi) &= \xi^2(\xi - 1).
\end{aligned}
$$

Both interpolation formulas (3) and (4) are tensor products of the 1-D basis functions [26] and can be extended directly to 3-D. In 3-D, the linear Lagrange interpolation function has eight terms and the cubic Hermite formula has 64.

Because the nodal derivatives in (4) are taken with respect to the finite element coordinate system, interelement gradient continuity will only be maintained if the element sides all have the same length. This restriction can be lifted if derivatives with respect to the globally continuous arc lengths of the element sides (s_l) rather than the finite element coordinates are used as the global parameters [25]. However, these new parameters cannot be used in (4). The required nodal derivatives are recovered in the process of mapping global to element parameters by multiplying the global parameters by constant scaling factors $ds_l/d\xi_l$ that are defined for each element side

$$
\begin{aligned}
\frac{\partial z}{\partial \xi_1} &= \frac{\partial z}{\partial s_1}\frac{ds_1}{d\xi_1} \\
\frac{\partial z}{\partial \xi_2} &= \frac{\partial z}{\partial s_2}\frac{ds_2}{d\xi_2} \\
\frac{\partial^2 z}{\partial \xi_1 \partial \xi_2} &= \frac{\partial^2 z}{\partial s_1 \partial s_2}\frac{ds_1}{d\xi_1}\frac{ds_2}{d\xi_2}. \qquad (5)
\end{aligned}
$$

Since the element sides are always of unit length in the finite element coordinate system, the scaling factors are simply the arc length of the element sides in the global coordinate system.

Both interpolation formulas (3) and (4) can be written more compactly by defining multidimensional element basis functions Ψ_μ as the 1-D basis function *products* that multiply the nodal parameters. For example, for bilinear Lagrange interpolation, $\Psi_1(\xi_1, \xi_2) = L_1(\xi_1)\, L_1(\xi_2)$, $\Psi_2(\xi_1, \xi_2) = L_2(\xi_1)\, L_1(\xi_2)$, etc. The mapping from global to element parameters can be written as $\hat{z}^{\mu(\epsilon)} = \Gamma_b^{\mu(\epsilon)} Z^b$. In this expression, the index ϵ identifies a particular finite element. This index differs from the others in this paper in that it is never summed. The index μ ranges over the individual 2-D basis functions ($1, \cdots, 4$ for bilinear Lagrange interpolation and $1, \cdots, 16$ for bicubic Hermite interpolation), and b ranges over all global degrees-of-freedom (i.e., global parameters) in the finite element approximation. For a given element ϵ, $\hat{z}^{\mu(\epsilon)}$ is the vector of element parameters (i.e., z and its derivatives in (3) and (4)), and $\Gamma_b^{\mu(\epsilon)}$ is a matrix that maps each element parameter μ to a single global parameter b. For linear Lagrange interpolation, each nonzero matrix entry is 1.0, so that the matrix simply specifies the connectivity of the elements. For Hermite interpolation, the nonzero entries are the derivative scaling factors in (5). Z^b is the vector of all global parameters. Using this notation, the value of z at point $\boldsymbol{\xi}$ in element ϵ is given by

$$
z(\boldsymbol{\xi}) = \psi_\mu(\boldsymbol{\xi})\hat{z}^{\mu(\epsilon)} = \psi_\mu(\boldsymbol{\xi})\Gamma_b^{\mu(\epsilon)} Z^b. \qquad (6)
$$

If the approximated variable is time-dependent, the global parameters become functions of time. Thus, the approximations for the excitation and recovery variables (u and v, respectively) are

$$
\begin{aligned}
u(\boldsymbol{\xi}, t) &= \Psi_\mu(\boldsymbol{\xi})\Gamma_b^{\mu(\epsilon)} U^b(t) \\
v(\boldsymbol{\xi}, t) &= \Psi_\mu(\boldsymbol{\xi})\Gamma_b^{\mu(\epsilon)} V^b(t). \qquad (7)
\end{aligned}
$$

Cubic Hermite interpolation is always used for u and v. This choice is mandated by our use of the collocation method (see below). Since these fields are time-dependent, the initial values of the global nodal parameter vectors U^b and V^b are defined at the start of each simulation and are then evolved in time. The global parameters defining the geometry, structure, and material properties of the mesh are fixed in time. In this paper, linear Lagrange interpolation is used for these variables, but the use of Hermite interpolation is available for more complex fields [27].

C. Transformation of the Governing Equations

In component form, (2) becomes

$$
\begin{aligned}
\frac{\partial u}{\partial t} &= \frac{\partial}{\partial x_i}\left(D^{ij}\frac{\partial u}{\partial x_j}\right) \\
&\quad + c_1 u(u - a)(1 - u) - c_2 uv \\
\frac{\partial v}{\partial t} &= b(u - dv). \qquad (8)
\end{aligned}
$$

These equations are transformed to simplify the diffusion tensor D^{ij} and to express the spatial derivatives of u in terms of the finite element coordinate system.

Several identities from tensor calculus [24] are required. If φ^a and $\overline{\varphi}^\alpha$ are the components of two general coordinate systems, z is a scalar field, t_a is a vector field, and δ_{ab} is the Kronecker delta, then

$$
\begin{aligned}
\frac{\partial z}{\partial \varphi_a} &= \frac{\partial z}{\partial \overline{\varphi}_\alpha}\frac{\partial \overline{\varphi}^\alpha}{\partial \varphi_a} \\
\frac{\partial \varphi^a}{\partial \overline{\varphi}_\alpha}\frac{\partial \overline{\varphi}^\alpha}{\partial \varphi_b} &= \frac{\partial \overline{\varphi}^\alpha}{\partial \varphi_b}\frac{\partial \varphi^a}{\partial \overline{\varphi}_\alpha} = \frac{\partial \varphi^a}{\partial \varphi_b} = \delta_{ab} \\
t_a \delta_{ab} &= t_b. \qquad (9)
\end{aligned}
$$

These identities can be used to show that

$$\frac{\partial^2 z}{\partial\varphi_a\partial\varphi_b} = \frac{\partial}{\partial\varphi_a}\left(\frac{\partial z}{\partial\varphi_b}\right) = \frac{\partial\overline{\varphi}^\alpha}{\partial\varphi_a}\frac{\partial}{\partial\overline{\varphi}_\alpha}\left(\frac{\partial\overline{\varphi}^\beta}{\partial\varphi_b}\frac{\partial z}{\partial\overline{\varphi}_\beta}\right) = \frac{\partial^2 z}{\partial\overline{\varphi}_\alpha\partial\overline{\varphi}_\beta}\frac{\partial\overline{\varphi}^\alpha}{\partial\varphi_a}\frac{\partial\overline{\varphi}^\beta}{\partial\varphi_b} + \frac{\partial z}{\partial\overline{\varphi}_\alpha}\frac{\partial^2\overline{\varphi}^\alpha}{\partial\varphi_a\partial\varphi_b}. \quad (10)$$

In (8), the components of the diffusion tensor (D^{ij}) are implicitly referred to the base vectors of the global Cartesian coordinate system. Because the muscle fiber orientation may be nonuniform, these components are functions of the global coordinates x^i. If the diffusive term in (8) is transformed to the fiber coordinate system, the component matrix of the diffusion tensor (now denoted $\hat{D}^{qr}$) becomes diagonal, and the components are simply the diffusion constants in the fiber and transverse directions. This transformation is achieved by making the substitution

$$D^{ij} = \hat{D}^{pq}\frac{\partial x^i}{\partial\nu_p}\frac{\partial x^j}{\partial\nu_q}$$

and using identities (9) and the chain rule. Thus,

$$\frac{\partial}{\partial x_i}\left(D^{ij}\frac{\partial u}{\partial x_j}\right) = \hat{D}^{pq}\left(\frac{\partial^2 x^i}{\partial\nu_r\partial\nu_p}\frac{\partial\nu^r}{\partial x_i}\frac{\partial u}{\partial\nu_q} + \frac{\partial^2 u}{\partial\nu_p\partial\nu_q}\right). \quad (11)$$

Since the finite element basis functions are defined in terms of the element coordinates ξ^l, the spatial derivatives of u must be transformed once again to this system. Using identities (9) and (10) on (11) and substituting back into (8), we obtain

$$\frac{\partial u}{\partial t} = A^l\frac{\partial u}{\partial\xi_l} + B^{lm}\frac{\partial^2 u}{\partial\xi_l\partial\xi_m} + c_1 u(u-a)(1-u) - c_2 uv$$
$$\frac{\partial v}{\partial t} = b(u - dv) \quad (12)$$

where

$$A^l = B^{lm}\frac{\partial^2 x^i}{\partial\xi_n\partial\xi_m}\frac{\partial\xi^n}{\partial x_i} + \hat{D}^{pq}\frac{\partial^2\xi^m}{\partial\nu_p\partial\nu_r}\frac{\partial\nu^r}{\partial\xi_m}\frac{\partial\xi^l}{\partial\nu_q} + \hat{D}^{pq}\frac{\partial^2\xi^l}{\partial\nu_p\partial\nu_q}$$

and

$$B^{lm} = \hat{D}^{pq}\frac{\partial\xi^l}{\partial\nu_p}\frac{\partial\xi^m}{\partial\nu_q}.$$

The first and second derivatives of several coordinate transformations appear in (12). Because the geometry of the mesh is defined using finite element interpolation, the global coordinates x^i of any point in the mesh are known functions of the finite element coordinates ξ^l, and the derivatives $\partial x^i/\partial\xi_l$ and $\partial^2 x^i/\partial\xi_l\partial\xi_m$ are easily computed. $\partial\xi^l/\partial x_i$ is obtained by inverting the matrix $\partial x^i/\partial\xi_l$. The derivatives involving the ν^p coordinates, although more complex, are also computed from the finite element description of the mesh's geometry and fiber field (Appendix).

D. The Finite Element Equations

Recall that the solution to the modified FHN system is expressed in terms of vectors of 1-D time-dependent functions $U^b(t)$ and $V^b(t)$ with known initial values (7). Since the primary task of our method is to evolve these functions in time, we must derive one ordinary differential equation (ODE) for each function. The collocation method [28] is an efficient way to accomplish this. In collocation, the approximate solution is made to satisfy the governing partial differential equations exactly at a discrete set of points. The form of the collocation equations is obtained by substituting (7) into (12)

$$\Psi_\mu\Gamma_b^{\mu(\epsilon)}\frac{dU^b}{dt} = \left(A^l\frac{\partial\Psi_\mu}{\partial\xi_l} + B^{lm}\frac{\partial^2\Psi_\mu}{\partial\xi_l\partial\xi_m}\right)\Gamma_b^{\mu(\epsilon)}U^b + c_1\Psi_\mu\Gamma_b^{\mu(\epsilon)}U^b(\Psi_\sigma\Gamma_c^{\sigma(\epsilon)}U^c - a)\cdot(1 - \Psi_\omega\Gamma_d^{\omega(\epsilon)}U^d) - c_2\Psi_\mu\Gamma_b^{\mu(\epsilon)}U^b\Psi_\omega\Gamma_c^{\omega(\epsilon)}V^c$$
$$\Psi_\mu\Gamma_b^{\mu(\epsilon)}\frac{dV^b}{dt} = b(\Psi_\mu\Gamma_b^{\mu(\epsilon)}U^b) - bd(\Psi_\mu\Gamma_b^{\mu(\epsilon)}V^b). \quad (13)$$

One of each of these equations is formed at each collocation point. The index ϵ specifies the element containing the collocation point. At any instant, the U^b and V^b vectors, the parameter maps $\Gamma_b^{\mu(\epsilon)}$, and the values and derivatives of the basis functions ψ_μ, which are evaluated at the ξ coordinates of the collocation point, are known, but the vectors dU^b/dt and dV^b/dt are unknown. Thus, the right-hand side of each of the above equations sums to a known scalar, and the products $\Psi_\mu\Gamma_b^{\mu(\epsilon)}(dU^b/dt)$ and $\Psi_\mu\Gamma_b^{\mu(\epsilon)}(dV^b/dt)$ are inner products of known and unknown vectors. If we assume for the moment that there are as many collocation points as there are degrees-of-freedom in the approximations of u and v, then the set of collocation equations forms two linear systems $\boldsymbol{A}\dot{\boldsymbol{U}} = \boldsymbol{b}$ and $\boldsymbol{A}\dot{\boldsymbol{V}} = \boldsymbol{b}$, where the finite element matrix $\boldsymbol{A}$ is the union of the vectors $\Psi_\mu\Gamma_b^{\mu(\epsilon)}$ and the vectors $\boldsymbol{b}$ and $\boldsymbol{c}$ are the unions of the right-hand sides of the collocation equations. These systems can be solved for dU^b/dt and dV^b/dt which can then be integrated in time providing a solution to the governing equations.

This scheme is appealing because there are no basis function products in the finite element matrix. As a result, collocation yields much sparser matrices than the more common Galerkin method [28]. In two dimensions, cubic Hermite interpolation uses four parameters per global node. Therefore, in the interior of a mesh, the number of collocation points matches the number of degrees-of-freedom if there are four collocation points per element (i.e., if one nodal parameter is assigned to each of the four elements surrounding a node). Cubic interpolation is the lowest degree that supports such a distribution scheme. The optimal locations of the collobation points have been shown to be at the roots of the Legendre polynomials [29]. Global convergence for collocation has been shown to be $O(h^2)$—which is comparable with the Galerkin method,

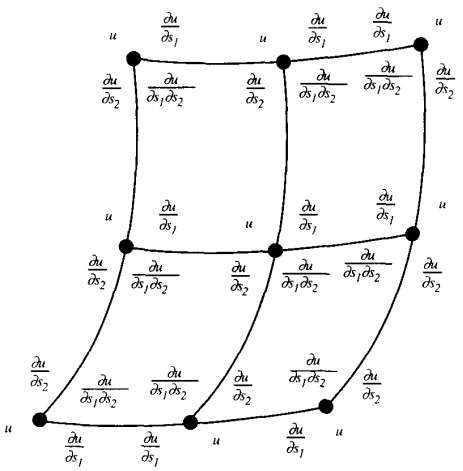

Fig. 4. The distribution of global parameters between the collocation and Galerkin methods. Each node is surrounded by its four parameters. Collocation equations are generated for the parameters located *inside* the mesh. These parameters are written on the approximate locations of the collocation points. The basis functions associated with the parameters *outside* the mesh support the approximation of u on the boundary, and Galerkin equations are formed for these parameters.

although at the collocation points, convergence is $O(h^4)$ [30], [29].

This scheme fails, however, at the boundaries, where there are fewer collocation points than nodal parameters. Also, this scheme does not enforce the boundary conditions. We resolve both of these problems by identifying the basis subset that supports the solution at the boundary and using the boundary conditions to form Galerkin finite element equations [31] for the associated global parameters. In the Galerkin method, the error in the solution is weighted with each basis function and integrated over the domain. Thus, when all of the Galerkin equations are satisfied, the error in the solution is orthogonal to the basis set from which the solution is constructed. In this application, the error is the flux of u, which is integrated only over the boundary of the domain. On most practical meshes, the number of equations generated in this way is exactly equal to the shortfall from collocation, thus ensuring a well-posed problem. However, on some meshes, this method results in too many equations, in which case we use all of the Galerkin equations, and remove enough collocation points to restore the balance between equations and unknowns. The distribution of parameters between the two types of equations is illustrated in Fig. 4. In a simpler scheme [28], the boundary degrees-of-freedom can be eliminated from the system without the use of the Galerkin method if the element corners are right-angled. However, we have not adopted this technique as this condition is too restrictive to accurately model the complex geometry of the heart.

The Galerkin equations for the excitation variable are derived by differentiating the no-flux boundary condition with respect to time

$$\frac{\partial}{\partial t}\left(\frac{\partial u}{\partial \boldsymbol{n}}\right) = \frac{\partial}{\partial t}\left(\frac{\partial \xi^{(l)}}{\partial x_i}\frac{\partial \xi^{m}}{\partial x_i}\frac{\partial u}{\partial \xi_m}\right) = 0. \tag{14}$$

Here, $\partial\xi^{(l)}/\partial x_i$ is the single contravariant base vector of the finite element coordinate system that is normal to the boundary. The set of basis functions that supports the solution on the boundary of each element $\psi_\sigma \Gamma_c^{\sigma(\epsilon)}$ is identified. Next, the first equation of (7) is substituted into (14), and the result is weighted with each function and integrated over the boundary

$$\left(\int_{\partial\Omega} \frac{\partial \xi^{(l)}}{\partial x_i}\frac{\partial \xi^{m}}{\partial x_i}\frac{\partial \Psi_\mu}{\partial \xi_m}\Psi_\sigma \, dS\right) \cdot \Gamma_b^{\mu(\epsilon)}\Gamma_c^{\sigma(\epsilon)}\frac{dU^b}{dt} = 0. \tag{15}$$

Note that since the index c is free, but does not run over all degrees-of-freedom in the approximation, and all quantities are known except dU^b/dt, (15) is an underdetermined, homogeneous system of linear equations. This system, together with the underdetermined system formed by the first of collocation equations (13) forms a completely determined linear system in the unknown vector dU^b/dt.

Boundary Galerkin equations must also be derived for the recovery variable v. Since there are no boundary conditions on v, one way to obtain the Galerkin equations is to derive them directly from the second part of (8)

$$\begin{aligned}\left(\int_{\partial\Omega} \Psi_\mu \Psi_\sigma \, dS\right)\Gamma_b^{\mu(\epsilon)}\Gamma_c^{\sigma(\epsilon)}\frac{dV^b}{dt} &= b\left(\int_{\partial\Omega} \Psi_\mu \Psi_\sigma \, dS\right)\Gamma_b^{\mu(\epsilon)}\Gamma_c^{\sigma(\epsilon)}U^b \\ &\quad - bd\left(\int_{\partial\Omega} \Psi_\mu \Psi_\sigma \, dS\right)\Gamma_b^{\mu(\epsilon)}\Gamma_c^{\sigma(\epsilon)}V^b.\end{aligned} \tag{16}$$

Alternately, a no-flux boundary condition can be imposed on v, yielding Galerkin equations similar to (15)

$$\left(\int_{\partial\Omega} \frac{\partial \xi^{(l)}}{\partial x_i}\frac{\partial \xi^{m}}{\partial x_i}\frac{\partial \Psi_\mu}{\partial \xi_m}\Psi_\sigma \, dS\right) \cdot \Gamma_b^{\mu(\epsilon)}\Gamma_c^{\sigma(\epsilon)}\frac{dV^b}{dt} = 0. \tag{17}$$

The latter scheme is advantageous in that it produces a coefficient matrix for dV^b/dt that is identical to the one for dU^b/dt, and as a result, only one finite element matrix must be stored and factorized. The latter scheme was used in all simulations in this paper.

The integrals in (15) and (16) or (17) are evaluated with a Gaussian quadrature scheme. The linear system (which is sparse) is solved using the Y12m package [32]. The resulting system of ODE's that governs U^b and V^b is evolved using a Runge–Kutta method (NAG routine D02BBF) that automatically and adaptively selects the size of the time step. It is important to note that the coefficient matrix of dU^b/dt and dV^b/dt does not contain any terms that are functions of time. Therefore, the linear system only needs to be factorized once, before the beginning of the time integration, and not at every timestep, for a considerable gain in computational efficiency. The sparseness of the finite element matrix due to the use of the collocation method adds to the efficiency of the method. Because the Galerkin equations are formulated in a space one dimension lower than the interior collocation equations (i.e.,

TABLE I
MEMBRANE PARAMETERS

a	0.13
b	0.013
c_1	0.26
c_2	0.1
d	1.0
$D_{longitudinal}$	
isotropic	1.0
anisotropic	4.0
$D_{transverse}$	1.0

the boundary), our use of the Galerkin method does not upset the sparsity of the finite element matrix.

E. Implementation

This computational method was implemented on a DEC-station 5000/200 workstation (Digital Equipment Corp., Maynard, MA) within the framework of a general-purpose finite element program used previously for other cardiac modeling applications [33]. To improve computational performance on complex meshes, a distributed implementation was developed. Problem setup and finite element matrix assembly were performed on the local workstation. The assembled matrices were then sent over the network to a remote Cray Y-MP 8/864 (Cray Research Inc., Eagan, MN) which factorized the matrices and integrated the system of ODE's. Only a single processor of the Cray was used. The solution was periodically sent back to the workstation for processing and/or output. The UNIX socket abstraction was used for communication between the two machines. Once the communication link had been established between the two systems, it was transparent to the user.

F. Choice of Membrane Parameters, Convergence, and Numerical Stability

To find appropriate membrane parameters and element sizes, solutions to (2) were obtained on a series of square, isotropic finite element meshes. For these tests, straight, uniform waves were initiated by setting u to 1.0 on the row of nodes along one edge of the mesh. All other nodal parameters for u and v were initially set to 0.0. The diffusion constants were set to unity, and the membrane parameters a, b, c_1, c_2, and d were manipulated by trial and error to produce a traveling-wave solution (Fig. 1(b)). Care was taken to make the decay in the recovery variable follow the recovery of the excitation variable as closely as possible. The membrane parameters, which were used in all subsequent simulations reported in this paper, are listed in Table I. Since the governing equations are dimensionless, the results of these simulations, and the others in this paper, are reported in terms of arbitrary "time units" and "space units." The correspondence between these units and physical units is discussed at the end of this section.

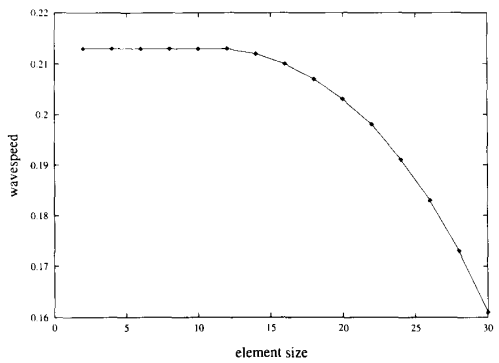

Fig. 5. Wavespeed convergence with increasing mesh refinement. As the size of the elements decreased, the speed of straight, uniform waves converged to 0.213 space units/time unit. All elements used in this paper were 10×10 space units or smaller.

The membrane parameters define the shape of the action potential pulse, e.g., the slope of the upstroke and the width of the pulse. The finite element mesh must be sufficiently refined so that at any instant in time, there are enough elements across the width of the pulse to faithfully represent it. The required number of elements is determined by the steepest part of the pulse, which is generally the upstroke. In a continuum model such as this, the wavespeed is a function of the upstroke velocity [34]. Therefore, to find the optimal element size for given parameter set, the element size should be decreased until wavespeed converges. When this has occurred, the mesh is sufficiently refined to accurately represent the upstroke, and hence, the entire action potential waveform.

This procedure was carried out for the parameter set in Table I. Wavespeed converged to 0.213 space units/time unit (Fig. 5) at an element size of between 12 and 14 space units. In the simulations reported in this paper, all elements were 10×10 space units, or smaller, which is well below the convergence threshold. Increasing the diffusion constants is equivalent to shrinking the elements. Therefore, anisotropic domains were created by increasing the longitudinal diffusion constant rather than by decreasing the transverse constant, thereby maintaining convergence in both directions.

The nature of the error due to the collocation method is illustrated in Fig. 6. Because the approximate solution is made to satisfy the governing equations exactly at discrete points, the error in the solution is not uniformly distributed. As the wavefront propagates, its location relative to the collocation points changes, and the solution oscillates (Fig. 6(a)). However, when the element size is within the convergence threshold used for all subsequent simulations (10×10 space units), the oscillation is essentially eliminated (Fig. 6(b)).

To further verify the implementation, the action potential waveforms were compared with waveforms generated by a simple finite difference program run with the same membrane parameters. In addition, the membrane parameters c_1, c_2, and b were set to zero, reducing (2) to the time-dependent diffusion equation. The same initial condition as above was given, and the asymptotic decay of u to a uniform level was compared with the analytic solution.

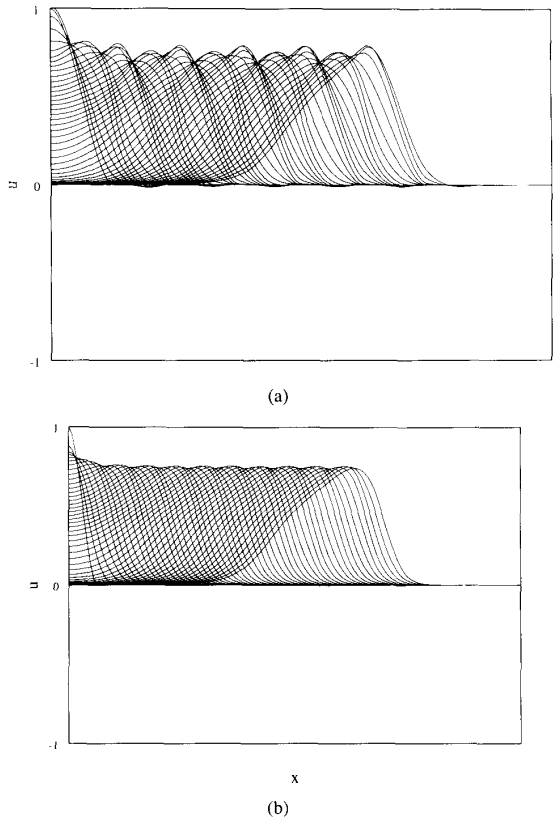

Fig. 6. Reduction of action potential oscillation by spatial mesh refinement. Rectangular, isotropic, 160×160 space unit meshes were stimulated along one edge to produce uniform, straight wavefronts. Snapshots of the u waveform were taken every ten time units for 500 time units and overlaid on the same axis. In (a), the elements were each 20×20 space units, and in (b) they were each 10×10 space units.

The attributes of the converged waves used in these tests can be used to establish a correspondence between the dimensionless time and space units used in this paper and physical dimensions. Assigning an experimental action potential duration of 205.0 ms [35] to the model's action potential duration (at 90% repolarization) of 325.0 time units maps one time unit to 0.63 ms. Similarly, assigning a longitudinal propagation velocity of 0.34 mm/ms [35] to the model's converged wavespeed of 0.213 space units/time unit maps one space unit to 0.99 mm. Assuming an action potential amplitude of 110 mV [35], with this time scale, the action potential upstroke of the model maps to 2.2 V/s. This is considerably smaller than typical experimental values of 100–200 V/s [34].

G. Computational Performance

To characterize the computational performance of our method, straight waves were propagated for 150 time units (95 ms using the above mapping) on 16×16 element meshes composed of 10×10 space unit elements. This area is roughly comparable to the epicardial surface of both ventricles of a canine heart. On the DECstation, 4.5 s of CPU time were required to assemble the finite element equations, and 10.9 s to factorize the finite element matrix. These costs are fixed for a simulation of any duration. Integrating the solution for the specified time required 55.3 s. When the Cray was used, the factorization time dropped to 2.0 s, and the solution time to 3.5 s. For comparison, the same solution was calculated on the DECstation using a finite difference program. This program used the same time-integrating scheme as the finite element code, but standard center differences were used for the spatial discretization. The mesh was refined to approximately the same place on its convergence curve (120×120 nodes) as the finite element mesh. The integration time for this program was 169 s, which is considerably longer than the total time used by the finite element method.

The solution time for the finite element method—exclusive of the cost of assembly and matrix factorization—is dominated by the repeated backsubstitution of the factorized matrix. To first order, the timing of this process is proportional to the number of nonzero elements in the matrix. In 2-D, the number of rows in the matrix is four times the number of nodes in the mesh. Each collocation equation has 16 terms (the number of basis functions that support the solution at a particular point within an element). The Galerkin equations have a variable bandwidth, but are somewhat less dense since they are formulated over the 1-D boundary. Therefore, the finite element matrix has approximately $16 \times 4 \times n$ nonzeros, where n is the number of nodes. In 3-D, each node has eight associated parameters, and each collocation equation has 64 terms. The 3-D finite element matrices are correspondingly larger and denser, and solution times scale accordingly.

IV. Model Results

The following 2-D simulations illustrate the use of our numerical method and demonstrate that it, together with our modification of the FHN system, can simulate cardiac action potential propagation in both normal and pathological situations.

A. The Wenckebach Phenomenon

A wave propagating in an unrecovered excitable medium is slower than a wave propagating in a fully recovered medium [36]. When applied to periodic wavetrains, this property is known as dispersion and is a consequence of the increased current required to bring refractory tissue to threshold. To test for the presence of dispersion in our model, a medium was stimulated at one end at short, constant intervals (Fig. 7). At the time of the second stimulus, the stimulation site (panel (a), left edge) was not fully recovered, and the second pulse was slowed by the refractory wake of the first pulse. As a result, by the end of the second interval (panel (b)), the stimulation site was even less recovered than it had been at the end of the first interval (panel (a)). The refractoriness of the stimulation site caused the third pulse to block completely (panel (c)), and the resulting "hole" in the wavetrain made it possible for the fourth pulse to propagate at nearly the same speed as the first (panel (d)). This cycle, in which every third pulse is unable to propagate, is characteristic of 3 : 2 Wenckebach periodicity (two responses for every three

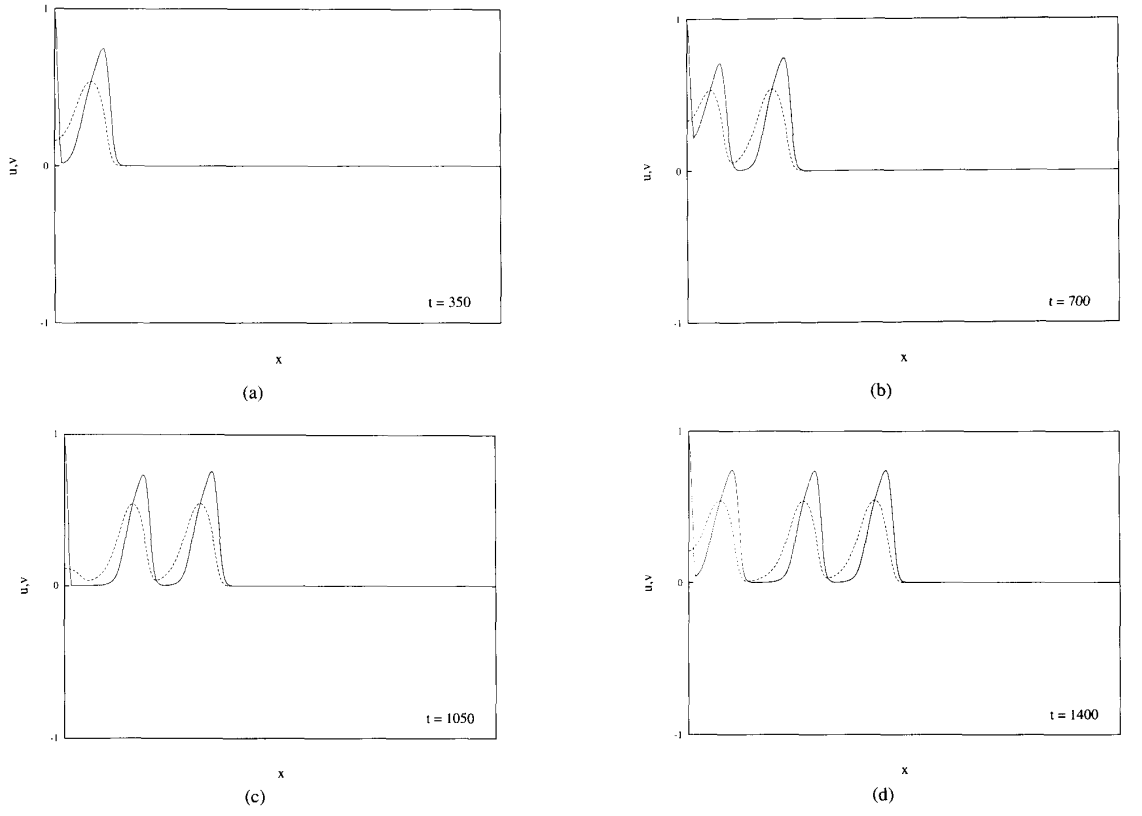

Fig. 7. Wenckebach periodicity in a wavetrain propagating down a long, thin mesh (640 × 10 space unit). The short coupling interval (350 time units) causes dispersive slowing of the second pulse (a), (b) and the failure of the third (c). The fourth pulse propagates successfully (d).

stimuli) [37]. Differing dynamics can be produced by varying the interval between stimuli.

B. The Effect of Wavefront Curvature

The effect of the curvature of a traveling wavefront on the velocity of propagation and the stability of the wave was studied by stimulating across the neck of a funnel-shaped domain (Fig. 8). Because of the no-flux boundary condition, the waves must intersect the boundaries at a right angle. Therefore, the wave propagating in the straight-sided region was straight, while the wave in the expanding region was curved. Since the curved wavefront was constantly expanding, each segment along it must excite a slightly longer segment ahead of it. Thus, the curved wavefront had a higher current load than the straight one, and consequently had a lower propagation velocity. In this example, the wavefront curvature was convex. In the case of concave curvature, this mechanism operates in reverse, making curved waves faster than straight ones. This result is consistent with singular perturbation analysis of excitable media [36] which predicts that wavespeed is linearly related to wavefront curvature.

A further consequence of wavefront curvature was studied by incorporating a funnel-like expansion into a loop (Fig. 9). The wave propagating into the expansion was slowed (panel (a), top left) as in the previous simulation (Fig. 8). However, in this case, the current load imposed by the wavefront curvature was great enough to cause the wave to progressively fade away (decremental conduction). This is an example of unidirectional block caused by geometric constraints on the shape of the wave. The surviving wave continued propagating around the loop in the clockwise direction, and finally reentered the

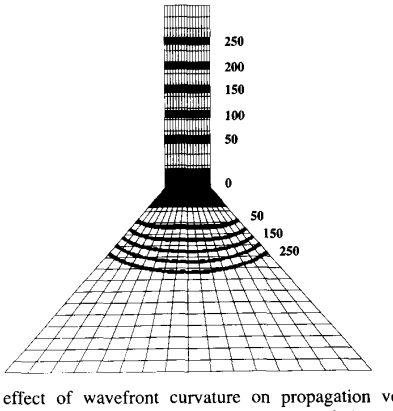

Fig. 8. The effect of wavefront curvature on propagation velocity. The convex curvature of the lower wave reduces its speed relative to the straight wave. Each contour stripe includes a small range of activation times, so the width of the stripe is roughly proportional to the local wavespeed. The mesh is 160 space units high and 160 space units across the base.

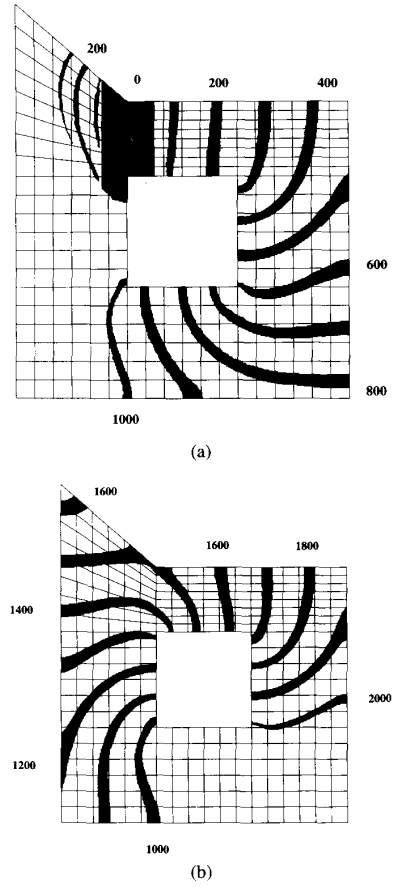

Fig. 9. Reentrant propagation around a fixed geometric obstacle. Block of the counterclockwise wave is caused by the sudden expansion of the domain at the stimulation site. The clockwise wave survives (a) and reenters the stimulation site from the retrograde direction (b). The mesh is 166 space units high and 140 space units wide.

constriction to begin a second circuit (panel (b)). Note that although the wave could not successfully propagate from the narrow to the wide side of the constriction, it was able to propagate through the constriction in the opposite direction. This simulation can be viewed as a model of large-scale reentry around a fixed geometric obstacle such as an apical aneurysm. The geometric constriction which causes the unidirectional block initiating the reentrant circuit might be associated with a pattern of tissue scarring.

C. Anisotropy

The high velocity of longitudinal relative to transverse propagation is thought to be directional differences in effective resistivity [38]. Therefore, our method models anisotropy by using a larger diffusion constant in the fiber direction than the cross-fiber direction. It is trivial to show that scaling a diffusion constant is equivalent to stretching space by the square root of the scaling factor. This fact is consistent with Luther's classical equation [39], [40] which states that in excitable media, wavespeed = $c\sqrt{kD}$ where c is a constant, k is a first-order rate constant, and D is the diffusion constant. Therefore, provided that the no-flux boundaries are sufficiently far from the region of interest, activation patterns on an isotropic domain should map directly to stretched patterns on an anisotropic domain with a spatially uniform fiber orientation. For example, features which are circular on a 2-D isotropic domain should become elliptical on the corresponding anisotropic domain.

This was indeed the case for radial wavefronts propagating outward from a simulus at the center of a 320 × 320 space unit, 32 × 32 element mesh. Initially, the mesh was isotropic, and the activation contours were circular. With a uniform 0° (horizontal) fiber field, and the diffusion constant in the longitudinal direction set to 4.0, early activation contours were not truly elliptical because the initial stimulus was circular. However, the steady-state activation contours were 2:1 ellipses, with the long axis aligned with the fibers. To show that this result was repeatable even if the fibers were not aligned with the principal axes of the elements, the simulation was repeated with a uniform 30° fiber angle. The steady-state activation contours were again 2:1 ellipses, and were superimposable with the contours of the previous simulation.

D. Spiral Wave Reentry

Reentrant spiral waves that circulate around functional, rather than anatomical, obstacles are thought to underlie ventricular fibrillation [41], [1]. To verify that our model is able to reproduce such waves, an isotropic 320 × 320 space unit mesh was stimulated with a "broken wave" extending upward from the bottom edge of the mesh (Fig. 10(a)). As the spiral wave evolved, its tip traced out a stationary circle that neither moved nor changed shape with succeeding cycles [23]. Next, a uniform 30° fiber angle was defined, and the simulation was repeated. The spiral wavetip path was stationary as before, but was transformed into a 2:1 ellipse aligned with the fibers (Fig. 10(b)), further verifying our method for modeling anisotropy. In both simulations, the spiral wave period was approximately 1400 time units, or 882 ms. This is considerably longer than periods of 97–250 ms measured in isolated 2-D slices of ventricular tissue [42].

E. Nonuniform Fiber Orientation

To assess the effect of a spatially *nonuniform* fiber orientation, we propagated an initially straight transverse wave across a uniform fiber field (Fig. 11(a)), and nonuniform fiber fields in which the fibers curved away from (Fig. 11(b)) and toward (Fig. 11(c) and (d)) the advancing wavefront. Normally, our no-flux boundary conditions force wavefronts to intersect the boundaries at right angles. To eliminate this constraint, in all four simulations, the parameter c_1 was set to zero on the nodes along the left and right sides of the mesh, and varied linearly from zero to the nominal value on the immediately adjacent nodes. This turned the outer columns of elements into a current sink that decoupled the wave ends from the boundaries. When the fibers curved away from the wavefront (Fig. 11(b)), propagation was slower than when the fibers curved toward the wavefront (Fig. 11(c)). The uniform fiber case (Fig. 11(a)) was intermediate. In addition, increasing the

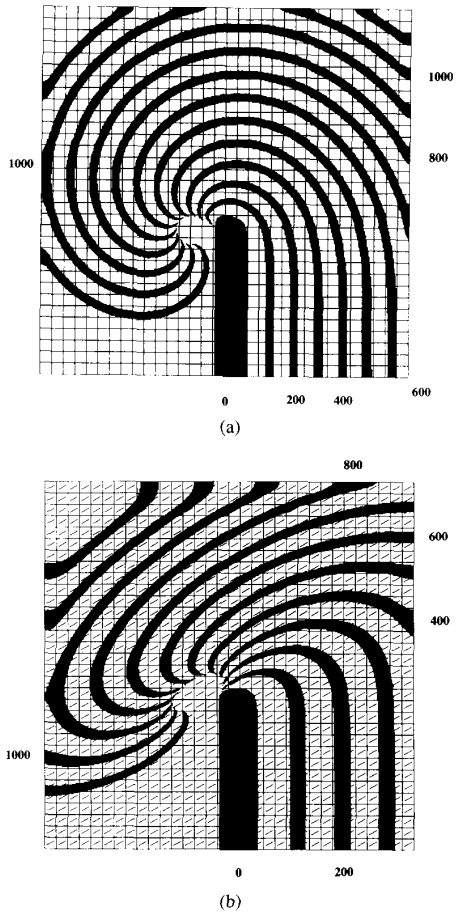

Fig. 10. Spiral wave reentry on isotropic (a) and anisotropic (b) meshes. Spiral waves were initiated from a broken wave stimulus, i.e., a wavefront that does not extend from one boundary to another, but instead has a free end within the mesh. In this type of reentry, the wave circulates around its own broken end rather than an anatomical obstacle as in Fig. 9. In both cases, the spiral wave period was approximately 1400 time units. In the isotropic case, the wave tip followed a repeating circular path. In the anisotropic case, the muscle fibers were aligned at a constant 30° angle from the horizontal (short hash marks), and the wave tip followed a repeating 2 : 1 elliptical path aligned with the fibers. The mesh was 320 × 320 space units.

fiber curvature further (Fig. 11(d)) caused the wave to conduct decrementally and eventually block.

V. Discussion

The primary purpose of this paper is to present a computational framework that will enable the effects of the heart's geometric complexity, fibrous architecture, and material heterogeneity on cardiac action potential propagation to be explored. We developed a novel hybrid collocation–Galerkin finite element method capable of taking these factors into account and used it to solve a new modification of the FitzHugh–Nagumo system (2). The solutions were shown to reproduce the essential qualities of impulse propagation. In a completely new result, nonuniformity of muscle fiber orientation was found to affect the propagation velocity and stability of wavefronts.

A. Numerical Procedures

The finite element method (FEM) [31] is a powerful tool for physiological modeling—in part because it allows the irregularities and inhomogeneities of biological systems to be modeled in a relatively straightforward way. Although FEM has been widely used since the 1960's in disciplines such as structural mechanics, it has only recently been applied to bioelectric phenomena [43]. Colli Franzone and colleagues have used standard FE techniques to model action potential propagation in an anisotropic block of myocardium [44]; however, in general, much simpler finite difference methods have been used [12], [14], [45]. Our timing benchmarks on a high-performance workstation indicate that our FEM implementation is more than two times faster than a program using a finite difference discretization. This comparison was somewhat unfair in that more attention was given to optimizing the FEM program; nevertheless, it points out the efficiency of the method.

In the finite element method, a known or unknown field is approximated over some spatial domain as a combination of interpolating basis functions. Known fields, such as the global coordinates of material points or local material properties, are defined by specifying the parameters of the basis functions. The parameters defining unknown fields, such as the excitation and recovery variables of the FHN system, must be calculated according to some criterion which determines how well the approximated solution satisfies the problem's governing equations. Generally, this optimizing criterion leads to a system of finite element equations. In our particular implementation, the finite element equations constitute a linear system with a time-dependent right-hand side. The solution of this system at any given point in time defines the first time derivatives of the unknown parameters of the excitation and recovery variables. These derivatives are used to integrate the action potential wave forward in time.

In our method, collocation, rather than the more commonly used Galerkin or variational methods, is used to formulate the finite element equations. Collocation has two primary advantages: 1) the assembled finite element equations are much sparser, and 2) collocation equations can be assembled faster [31]. The first point is the most significant because run time is dominated by the repeated triangular solution of the factorized finite element equations, and the time required for each solution is directly related to the sparsity of the linear system. The accuracy of the collocation and Galerkin methods have been shown to be comparable provided that the collocation points are located at the roots of the Legendre polynomials [29].

Pure collocation, however, also has several drawbacks relative to the other integral methods: it requires high-order basis functions, the error in the computed solution is not evenly distributed, and most importantly, the number of finite element equations it generates and the number of degrees-of-freedom in the finite element approximation do not automatically balance unless the mesh is infinite (has no boundaries). Other workers have resolved this problem by placing additional collocation points along the boundary or by restricting element cor-

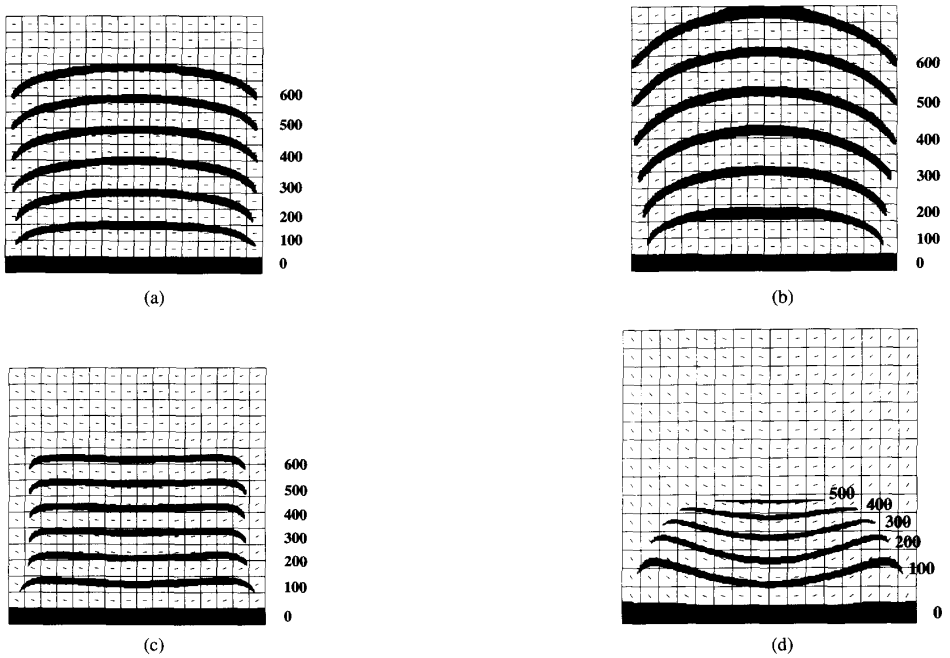

Fig. 11. The effect of nonuniform fiber orientation on wavespeed and stability. Nonuniformity of the fiber orientation slows (b) or speeds (c) propagation. The fiber curvature can also cause decremental conduction and block (d). Each mesh is 320×320 space units. In (a), the fiber orientation is a uniform $0°$. The fiber angle along the vertical edges of the mesh is $\pm 30°$ in (b) and (c) and $\pm 60°$ in (d). In each nonuniform case, the angle varies linearly across the mesh. The edges of each mesh are inexcitable, which decouples the wave ends from the boundary.

ners to 90° and eliminating the boundary degrees-of-freedom [28]. We found that these approaches were cumbersome or excessively restrictive, and instead chose to form Galerkin equations (based on boundary conditions, where possible) to satisfy the boundary degrees-of-freedom. Hence, in our hybrid method, interior degrees-of-freedom are satisfied with collocation equations, while boundary degrees-of-freedom are handled with Galerkin equations. This hybrid method should not be confused, however, with the collocation–Galerkin method proposed by Diaz [46] in which Galerkin equations were introduced to reduce the required polynomial order of the basis functions.

B. The Mathematical Model

The computational model presented in this paper was developed as a framework for studying cardiac action potential propagation on geometrically and structurally complex domains such as the heart. In principle, the method can be used to solve any model of impulse propagation in which the heart is regarded as a continuum. However, for simplicity, in this initial development, we have implemented a newly developed modification of the FitzHugh–Nagumo system of equations (2). Models of this type have been widely used [14], [47]–[49]; however, there is some doubt regarding their ability to *quantitatively* model the electrical activity of the heart [23]. Nevertheless, in our tests of the method, we show that it exhibits the essential properties of excitation, recovery, and refractoriness, and furthermore, can *qualitatively* reproduce many phenomena found in experimental, analytical, and computational studies. For example, the dependence of wavespeed on the refractoriness of the media (Fig. 7) and wavefront curvature (Figs. 8 and 9), large-scale reentry around a fixed obstacle (Fig. 9), and spiral wave (functional) reentry (Fig. 10).

The ability of this model to produce new information was illustrated when a spatially *non*uniform fiber field was introduced. As shown in Fig. 11, a transverse wave propagating across a nonuniform fiber field in which the fibers curve away from the wavefront (panel (b)) was slower than a wave traversing a uniform fiber field (panel (a)). Similarly, fibers curving toward the wavefront increased propagation velocity (panel (c)). It was also possible, by further increasing the fiber curvature, to cause propagation to fail completely (panel (d)). This behavior arises because, when the fiber orientation is nonuniform, the diffusive term in (1) $(\nabla \cdot \boldsymbol{D} \nabla u)$ expands into the first two terms on the right-hand side of (12). The first term takes into account the spatial variation of the principal axes of the diffusion tensor $\boldsymbol{D}$. The second term involves the spatial variation of the gradient of u. The wavespeed variations in Fig. 11 are dominated by the first term, which is nonzero only in the presence of fiber curvature. The diffusion tensor operates on the gradient vector of u to "tip" it into the direction of the fibers. Hence, when the fibers curve toward the wavefront, the nonuniformity of the diffusion tensor concentrates depolarizing current, increasing propagation velocity. When the fibers curve away from the wavefront, the opposite occurs. This phenomenon may have important implications to the dynamics of activation waves

in situ, and is experimentally testable, for example, in a thin epicardial tissue slice taken from the RV outflow tract where pronounced curvature is observed.

The model can be enhanced to yield more quantitative results in several ways. Much can be achieved simply by tuning the parameters of the present model. For example, the action potential upstroke produced by the current parameter set is too slow (Fig. 1(b)). By decreasing the element size, the parameters can be retuned to produce action potentials with physiological upstroke velocities, propagation velocities, and durations. In addition, tuning the parameters to increase the upstroke velocity implicitly increases the excitability of the medium. Since spiral wave period decreases as excitability is increased [12], correcting the upstroke velocity is also likely to decrease the spiral wave period produced by the model (Fig. 11) to a more physiological value. Nonlinear parameter optimization techniques [50] may be used to help automate this process. Improved fits to experimental data may also be achieved by modifying the functional form of the governing equations. In fact, the transformation of (1) to (2) is an example of such a modification. This simple alternation, which does not increase computational cost, vastly improves the shape of the waveform.

An alternative to the above phenomenological approach is to incorporate physiologically based models into the finite element framework. For example, electrotonic currents in the heart are not governed by the simple diffusion of a single "excitation variable" through a single domain; rather, the tissue is composed of two interpenetrating domains: the intracellular and extracellular spaces. Bidomain theory [51], [52] has been developed to account for the differing potentials in these two domains, and since its equations are continuous, it can be incorporated into the finite element framework. Second, the action potential is driven by complex biochemical events in the cell membrane involving the passive and active transport of several chemical species. FNH type models emulate this complexity with a simple two-state-variable oscillator. Higher level ionic models of the action potential exist [15], [16], and may be used to replace our simple kinetic.

A drawback of the finite element method is that it treats myocardium as a continuum, and therefore cannot take the discrete nature of the tissue into account. It has been shown that intracellular discontinuities can account for some directional differences in action potential parameters such as the maximum upstroke velocity, the time constant of the foot of the action potential, and the safety factor of propagation [34]. Although the discreteness of myocardium cannot be modeled directly by the finite element method, it is possible to model the effects of discreteness phenomenologically. For example, the membrane parameters might be made functions of the inner product between the local fiber angle and the wavefront normal vector. Such a scheme could introduce directional differences in action potential parameters without explicit consideration of the discreteness of the medium.

The manner in which the current model is extended will depend largely on the type of problem being solved. Two-dimensional solution times are currently quite modest—better, in fact, than competing finite difference methods—and it will be practical to incorporate a high degree of biophysical complexity in these models without exceeding current computing capacity. On the other hand, in 3-D problems, both the size and density of the finite element matrix grow dramatically, increasing both the memory and the solution time needed by the method. Phenomenological models will remain useful for practical simulations of global activation patterns on meshes with realistic geometries.

Appendix
Transformations Between the ξ and ν Coordinate Systems

In our geometric model of the heart, the muscle fibers are constrained to lie in planes perpendicular to the transmural coordinate axis. Thus, in both 2-D and 3-D problems, the fiber field is defined by a single angle taken with respect to a local finite element coordinate axis ξ^l. We define a locally orthonormal coordinate system $\boldsymbol{\nu}$ that at every point has one axis aligned with the fibers. At a point P, the covariant base vectors of the fiber and finite element coordinate systems ($\boldsymbol{a}_p$ and $\boldsymbol{g}_l$, respectively) are related by the transformation law [24]

$$\boldsymbol{a}_q = \beta_q^l \boldsymbol{g}_l \tag{A1}$$

where the transformation matrix β_q^l is defined at P by

$$\beta_q^l = \boldsymbol{a}_q \cdot \boldsymbol{g}^l = \left.\frac{\partial \xi^l}{\partial \nu_q}\right|_P \tag{A2}$$

where the $\boldsymbol{g}^l$ are the contravariant base vectors of the $\boldsymbol{\xi}$ system. The components of the transformation matrix are derived using the following conditions. First, the ν^1 and ν^2 axes lie in the same plane as the ξ^1 and ξ^2 axes and ν^3 is normal to this plane

$$\begin{aligned}
\boldsymbol{a}_1 \cdot \boldsymbol{g}^3 &= \frac{\partial \xi^3}{\partial v_1} = 0 \\
\boldsymbol{a}_2 \cdot \boldsymbol{g}^3 &= \frac{\partial \xi^3}{\partial v_2} = 0 \\
\boldsymbol{a}_3 \cdot \boldsymbol{g}^3 &= \frac{\partial \xi^3}{\partial v_3} = \sqrt{a_{33} g^{33}}
\end{aligned} \tag{A3}$$

where a_{qr} is the covariant metric tensor of the $\boldsymbol{\nu}$ system and g^{lm} is the contravariant metric tensor of the $\boldsymbol{\xi}$ system. Next, we choose orthonormal scaling for the $\boldsymbol{\nu}$ coordinate system

$$a_{qr} = \frac{\partial \xi^l}{\partial \nu_q} \frac{\partial \xi^m}{\partial \nu_r} g_{lm} = \delta_{qr}. \tag{A4}$$

Finally, $\boldsymbol{a}_1$ subtends angles η_1 and η_2 with $\boldsymbol{g}_1$ and $\boldsymbol{g}_2$

$$\begin{aligned}
\cos \eta_1 &= \frac{\boldsymbol{g}_1 \cdot \boldsymbol{a}_1}{|\boldsymbol{g}_1||\boldsymbol{a}_1|} = \frac{\partial \xi^m}{\partial \nu_1} \frac{g_{1m}}{\sqrt{g_{11} a_{11}}} \\
\cos \eta_2 &= \frac{\boldsymbol{g}_2 \cdot \boldsymbol{a}_1}{|\boldsymbol{g}_2||\boldsymbol{a}_1|} = \frac{\partial \xi^m}{\partial \nu_1} \frac{g_{2m}}{\sqrt{g_{22} a_{11}}}.
\end{aligned} \tag{A5}$$

These conditions are solved to give

$$\beta_q^l = \begin{bmatrix}
\dfrac{g_{22}K_1 - g_{12}K_2}{L^2} & \dfrac{-K_2}{L} & \sqrt{g^{33}}\dfrac{(g_{12}g_{23} - g_{22}g_{13})}{L^2} \\
\dfrac{g_{11}K_2 - g_{12}K_1}{L^2} & \dfrac{K_1}{L} & \sqrt{g^{33}}\dfrac{(g_{12}g_{13} - g_{11}g_{23})}{L^2} \\
0 & 0 & \dfrac{L^2}{\sqrt{g^{33}}}
\end{bmatrix} \tag{A6}$$

where

$$K_1 = \sqrt{g_{11}} \cos \eta_1$$
$$K_2 = \sqrt{g_{22}} \cos \eta_2 = \frac{g_{12}}{\sqrt{g_{11}}} \cos \eta_1 + \frac{L}{\sqrt{g_{11}}} \sin \eta_1$$
$$L^2 = g_{11}g_{22} - (g_{12})^2.$$

In the special case of an orthonormal finite element coordinate system (i.e., $g^{lm} = g_{lm} = \delta_{lm}$), (A6) reduces to a plane rotation

$$\beta_q^l = \begin{bmatrix} \cos \eta_1 & -\sin \eta_1 & 0 \\ \sin \eta_1 & \cos \eta_1 & 0 \\ 0 & 0 & 1 \end{bmatrix}. \tag{A7}$$

The matrix $\partial \nu^q / \partial \xi_l$ at P is obtained by inverting the right-hand side of (A6).

The fiber angle and the base vectors of the ξ system are functions of position. Therefore, in the neighborhood of point P, we have

$$\frac{\partial \xi^l}{\partial \nu_q} = \beta_q^l + \nu^r \frac{\partial}{\partial \nu_q}(\beta_r^l). \tag{A8}$$

Differentiating (A8) and keeping only leading order terms gives the second derivatives of the ξ^l coordinates with respect to the ν^q coordinates

$$\frac{\partial^2 \xi^l}{\partial \nu_q \partial \nu_r} = \frac{\partial}{\partial \nu_r}(\beta_q^l) + \frac{\partial}{\partial \nu_q}(\beta_r^l). \tag{A9}$$

REFERENCES

[1] P.-S. Chen *et al.*, "Mechanism of ventricular vulnerability to single premature stimuli in open-chest dogs," *Circ. Res.*, vol. 62, pp. 1191–1209, 1988.

[2] N. Shibata *et al.*, "Influence of shock strength and timing on induction of ventricular arrhythmias in dogs," *Amer. J. Physiol.*, vol. 255, pp. H891–H901, 1988.

[3] D. W. Frazier *et al.*, "Mechanism for electrical initiation of reentry in normal canine myocardium," *J. Clin. Invest.*, vol. 83, pp. 1039–1052, 1989.

[4] S. M. Pogwizd and P. B. Corr, "Mechanisms underlying the development of ventricular fibrillation during early myocardial ischemia," *Circ. Res.*, vol. 66, pp. 672–695, 1990.

[5] R. Plonsey and R. C. Barr, "Mathematical modeling of electrical activity of the heart," *J. Electrocardiol.*, vol. 20, pp. 219–226, 1987.

[6] R. M. Gulrajani, "Models of the electrical activity of the heart and computer simulation of the electrocardiogram," *Crit. Rev. Biomed. Eng.*, vol. 16, pp. 1–66, 1988.

[7] G. K. Moe *et al.*, "A computer model of atrial fibrillation," *Amer. Heart J.*, vol. 67, pp. 200–220, 1964.

[8] J. M. Smith and R. J. Cohen, "Simple finite element model accounts for a wide range of cardiac dysrhythmias," *Proc. Nat. Acad. Sci. USA*, vol. 81, pp. 233–237, 1984.

[9] N. V. Thakor and L. N. Eisenman, "Three-dimensional computer model of the heart: Fibrillation induced by extrastimulation," *Comput. Biomed. Res.*, vol. 22, pp. 532–545, 1989.

[10] M. Restivo *et al.*, "A logical state model of reentrant ventricular activation," *IEEE Trans. Biomed. Eng.*, vol. 37, pp. 344–353, 1990.

[11] M. Gerhardt *et al.*, "A cellular automaton model of excitable media including curvature and dispersion," *Science*, vol. 247, pp. 1563–1566, 1990.

[12] V. S. Zykov, *Simulation of Wave Processes in Excitable Media*. New York: Manchester Univ. Press, 1987.

[13] A. T. Winfree, *When Time Breaks Down*. Princeton, NJ: Princeton Univ. Press, 1987.

[14] ——, "Electrical instability in cardiac muscle: Phase singularities and rotors," *J. Theor. Biol.*, vol. 138, pp. 353–405, 1989.

[15] G. W. Beeler and H. Reuter, "Reconstruction of the action potential of ventricular myocardial fibers," *J. Physiol. (London)*, vol. 268, pp. 177–210, 1977.

[16] C.-H. Luo and Y. Rudy, "A model of the ventricular cardiac action potential: Depolarization, repolarization, and their interaction," *Circ. Res.*, vol. 68, pp. 1501–1526, 1991.

[17] R. C. Barr and R. Plonsey, "Propagation of excitation in idealized anisotropic two-dimensional tissue," *Biophys. J.*, vol. 45, pp. 1191–1202, 1984.

[18] C. S. Henriquez and R. Plonsey, "Simulation of propagation along a cylindrical bundle of cardiac tissue. 1. Mathematical formulation," *IEEE Trans. Biomed. Eng.*, vol. 37, pp. 850–860, 1990.

[19] ——, "Simulation of propagation along a cylindrical bundle of cardiac tissue. 2. Results of simulation," *IEEE Trans. Biomed. Eng.*, vol. 37, pp. 861–875, 1990.

[20] L. J. Leon and F. A. Roberge, "Structural complexity effects on transverse propagation in a two-dimensional model of myocardium," *IEEE Trans. Biomed. Eng.*, vol. 38, pp. 997–1009, 1991.

[21] B. J. Roth, "Action potential propagation in a thick strand of cardiac muscle," *Circ. Res.*, vol. 68, pp. 162–173, 1991.

[22] R. A. FitzHugh, "Impulses and physiological states in theoretical models of nerve membrane," *Biophys. J.*, vol. 1, pp. 445–466, 1961.

[23] A. T. Winfree, "Varieties of spiral wave behavior: an experimentalist's approach to the theory of excitable media," *Chaos*, vol. 1, pp. 303–334, 1991.

[24] Y.-C. Fung, *Foundations of Solid Mechanics*. Englewood Cliffs, NJ: Prentice-Hall, 1965.

[25] P. J. Hunter *et al.*, "An anatomical heart model with applications to myocardial activation and ventricular mechanics," *Crit. Rev. Biomed. Eng.*, vol. 20, pp. 403–426, 1992.

[26] J. T. Oden, *Finite Elements of Nonlinear Continua*. New York: McGraw-Hill, 1972.

[27] P. M. Nielsen *et al.*, "A mathematical model of the geometry and fibrous structure of the heart," *Amer. J. Physiol.*, vol. 260, pp. H1365–H1375, 1991.

[28] E. O. Frind and G. F. Pinder, "A collocation finite element method for potential problems in irregular domains," *Int. J. Mumer. Methods Eng.*, vol. 14, pp. 681–701, 1979.

[29] C. DeBoor and B. Swartz, "Collocation at Gaussian points," *SIAM J. Numer. Anal.*, vol. 10, pp. 582–606, 1973.

[30] S. N. Atluri, "Other finite element methods," in *Finite Element Handbook*, H. Kardestuncer, Ed. New York: McGraw-Hill, 1987, pp. 2.203–2.247.

[31] R. Wait and A. R. Mitchell, *Finite Element Analysis and Applications*. Chichester: Wiley, 1985.

[32] O. Osterby and Z. Zlatev, *Direct Methods for Sparse Matrices*. New York: Springer-Verlag, 1983.

[33] P. J. Hunter and B. H. Smaill, "The analysis of cardiac function: A continuum approach," *Prog. Biophys. Molec. Biol.*, vol. 52, pp. 101–164, 1988.

[34] M. S. Spach *et al.*, "The discontinuous nature of propagation in normal canine cardiac muscle: Evidence for recurrent discontinuities of intracellular resistance that affects membrane currents," *Circ. Res.*, vol. 48, pp. 39–54, 1981.

[35] C. Delgado *et al.*, "Directional differences in excitability and margin of safety for propagation in sheep ventricular epicardial muscle," *Circ. Res.*, vol. 67, pp. 97–110, 1990.

[36] J. J. Tyson and J. P. Keener, "Singular perturbation theory of traveling waves in excitable media (a review), " *Physica D*, vol. 32, pp. 327–361, 1988.

[37] J. Jalife and M. Delmar, "Ionic basis of the Wenckebach phenomenon," in *Theory of Heart: Biomechanics, Biophysics, and Nonlinear Dynamics of Cardiac Function*, L. Glass, P. J. Hunter, and A. D. McCulloch, Eds. New York: Springer-Verlag, 1991, pp. 359–376.

[38] M. S. Spach and J. M. Kootsey, "The nature of electrical propagation in cardiac muscle," *Amer. J. Physiol.*, vol. 244, pp. H3–H22, 1983.

[39] R. Arnold *et al.*, "Translation of Luther's propagation of chemical reactions in space," *J. Chem. Educ.*, vol. 64, pp. 740–742, 1987.

[40] K. Showalter and J. J. Tyson, "Luther's 1906 discovery and analysis of chemical waves," *J. Chem. Educ.*, vol. 64, pp. 742–744, 1987.

[41] M. A. Allessie *et al.*, "Circus movement in rabbit atrial muscle as a mechanism of tachycardia. III. The leading circle concept: A new model of circus movement in cardiac tissue without the involvement of an anatomic obstacle," *Circ. Res.*, vol. 41, pp. 9–18, 1977.

[42] A. M. Pertsov *et al.*, "Spiral waves of excitation underlie reentrant activity in isolated cardiac muscle," *Circ. Res.*, vol. 72, pp. 631–650, 1993.
[43] C. E. Miller and C. S. Henriquez, "Finite element analysis of bioelectric phenomena," *Crit. Rev. Biomed. Eng.*, vol. 18, pp. 207–233, 1990.
[44] P. Colli Franzone, "Spreading of excitation in 3-D models of the anisotropic cardiac tissue. I. Validation of the eikonal model," *Math. Biosci.*, vol. 113, pp. 145–209, 1993.
[45] B. Y. Kogan *et al.*, "Simulation of nonlinear distributed parameter systems on the connection machine," *Simulation*, vol. 15, pp. 271–288, 1990.
[46] J. C. Diaz, "A collocation-Galerkin method for the two point boundary value problem using continuous piecewise polynomial spaces," *SIAM J. Numer. Anal.*, vol. 14, p. 844, 1977.
[47] B. Y. Kogan *et al.*, "The simplified FitzHugh-Nagumo model with action potential duration restitution: Effects on 2-D wave propagation," *Physica D*, vol. 50, pp. 327–340, 1991.
[48] B. Y. Kogan *et al.*, "The role of diastolic outward current deactivation kinetics on the induction of spiral waves," *Pacing Clin. Electrophysiol.*, vol. 14, pp. 1688–1693, 1991.
[49] J. M. Davidenko *et al.*, "Stationary and drifting spiral waves of excitation in isolated cardiac muscle," *Nature*, vol. 355, pp. 349–351, 1992.
[50] P. E. Gill *et al.*, *Practical Optimization*. New York: Academic, 1981.
[51] L. Tung, "A bidomain model for describing ischemic myocardial d-c potentials," Ph.D. dissertation, Massachuesetts Inst. Technol., 1978.
[52] R. Plonsey and R. C. Barr, "Current flow patterns in two-dimensional anisotropic bisyncytia with normal and extreme conductivities," *Biophys J.*, vol. 45, pp. 557–571, 1984.

Jack M. Rogers was born in El Paso, TX, in 1963. He received the B.S., M.S., and Ph.D. degrees in bioengineering from the University of California, San Diego, in 1986, 1990, and 1993, respectively.

He has worked at the San Diego Supercomputer Center since 1986, where he is currently a Senior Research Scientist. His interests include cardiac electrophysiology and high-performance computing.

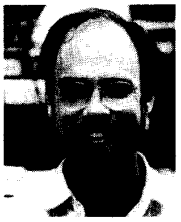

Andrew D. McCulloch was born in Auckland, New Zealand, in 1961. He received the B.E. (Hons) and Ph.D. degrees from the University of Auckland in 1981 and 1986, respectively.

He is now an Associate Professor of Bioengineering at the University of California, San Diego. He is also a member of the UCSD Institute for Biomedical Engineering and an NSF Presidential Young Investigator.